Acta Materialia 272 (2024) 119917

Contents lists available at ScienceDirect

Acta Materialia

journal homepage: www.elsevier.com/locate/actamat

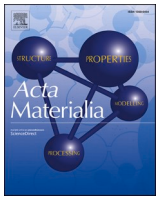

Full length article

Revealing *in situ* stress-induced short- and medium-range atomic structure evolution in a multicomponent metallic glassy alloy

Shifeng Luo [a,b,c,d,*], Jia Chuan Khong [c,e], Shi Huang [c], Guangyu Yang [b], Jiawei Mi [c,f,**]

[a] School of Materials Science and Engineering, Hefei University of Technology, Hefei 230009, PR China
[b] State Key Laboratory of Solidification Processing, Northwestern Polytechnical University, Xi'an 710072, PR China
[c] School of Engineering, University of Hull, Cottingham Road, Hull HU6 7RX, UK
[d] Engineering Research Center of High-Performance Copper Alloy Materials and Processing, Ministry of Education, Hefei University of Technology, Hefei 230009, PR China
[e] Department of Medical Physics & Biomedical Engineering, University College London, London WC1E 6BT, UK
[f] School of Materials Science and Engineering, Shanghai Jiao Tong University, Shanghai 200240, PR China

ARTICLE INFO

Keywords:
Short-range order
Medium-range order
Synchrotron x-ray total scattering
In situ electron microscopy imaging
Empirical potential structure refinement
Multiplecomponent glassy alloys

ABSTRACT

Deformation behaviour of multicomponent metallic glasses are determined by the evolution/reconfiguration of the short- and medium-range order (SRO and MRO) atomic structures. A precise understanding of how different atom species rearrange themselves in different stress states is still a great challenge in materials science and engineering. Here, we report a systematic and synergetic research of using electron microscopy imaging, synchrotron X-ray total scattering plus empirical potential structure refinement (EPSR) modelling to study *in situ* the deformation of a Zr-based multicomponent metallic glassy alloy with 5 elements. Systematic and comprehensive analyses on the characteristics of the SRO and MRO structures in 3D and the decoupled 15 partial PDFs at each stress level reveal quantitatively how the SRO and MRO structures evolve or reconfigure in 3D space in the tensile and compressive stress states. The results show that the Zr-centred atom clusters have low degree of icosahedra and are the preferred atom clusters to rearrange themselves under the tensile and compressive stresses. The Zr-Zr is the dominant atom pair in controlling the shear band's initiation and propagation. The evolution and reconfiguration of the MRO clusters under different stress states are realised by changing the connection modes between the Zr-centred atom clusters. The coordinated changes of both bond angles and bond lengths of the Zr-centred clusters are the dominant factors in accommodating the tensile or compressive strains. While other solute-centred MRO clusters only play minor roles in the atomic structure reconfiguration/evolution. The research has demonstrated a synergetic and multimodal materials operando characterization methodology that has great application potential in design and development of high performance multiple-component engineering alloys.

1. Introduction

Most crystalline and amorphous metallic alloys are multicomponent systems of more than three elements [1–4]. For crystalline alloy systems, multiple elements are needed to enable solute/precipitation strengthening, grain/phase boundary strengthening, or combination of these [5,6]. While for amorphous alloys or high-entropy alloy systems, multiple elements are mainly for enhancing either glass-forming ability or phase stability to achieve the designed mechanical or functional properties, i.e., strength, ductility, corrosion resistance, electronic and magnetic properties, etc. [7,8]. Quantitative description of the role of different atom species in the formation of different atomic/nano/micrometre structures and their effects on properties is still a great challenge in physical and materials science [9,10]. Currently, one of the most important research directions is to study and quantify the deformation and strengthening mechanisms of multicomponent amorphous or high-entropy alloy systems [11,12]. In this regard, high resolution scanning electron/transmission microscopy (SEM/TEM) equipped with high precision nano/micromechanical test rigs have been developed for imaging *in situ* the tensile/compression, bending/shearing and fatigue

* Corresponding author at: School of Materials Science and Engineering, Hefei University of Technology, Hefei 230009, PR China
** Corresponding author at: School of Engineering, University of Hull, Cottingham Road, Hull HU6 7RX, UK.
E-mail addresses: sfluo@hfut.edu.cn (S. Luo), J.Mi@hull.ac.uk (J. Mi).

https://doi.org/10.1016/j.actamat.2024.119917
Received 25 September 2023; Received in revised form 10 April 2024; Accepted 11 April 2024
Available online 12 April 2024
1359-6454/© 2024 The Authors. Published by Elsevier Ltd on behalf of Acta Materialia Inc. This is an open access article under the CC BY license (http://creativecommons.org/licenses/by/4.0/).

deformation of multicomponent alloys [13–17]. Such advanced instruments and real-space imaging methods have provided very rich real-time collected image data and new insights into the strengthening and deformation mechanisms of numerous multicomponent systems. For example, Cao et al. [18] studied *in situ* the link between tensile property and the pre-existing shear bands in a Zr-based metallic glass (MG) inside an SEM, and found that the properly spaced pre-existing shear bands lead to higher tensile plastic strain. Chen et al. [19] conducted *in situ* compression of MG micropillars and revealed that, in large-size pillars, the deformation is controlled by shear band nucleation. While, in small-size pillars, it is controlled by shear band propagation. The researchers in Mi's group have also carried out extensively *in situ* studies on the deformation behaviour of MGs and MG matrix composite as reported in [20–22]. However these real space imaging methods (unless the imaged features can be utilised in image correlation analysis) often have inherent difficulties in providing the local stress/-strain information associated with the deformed local structure features, e.g., around a shear band or an initiated crack as reported in [13–17]. It is virtually impossible, by using the imaging methods alone, to establish a quantitative link between the localized stress/strain field and the resulting atomic structure change in 3D space.

Poulsen et al. [23] have demonstrated that, using synchrotron X-ray total scattering (SXTS) method, the local atomic strain distribution of a tertiary amorphous alloy ($Mg_{60}Cu_{30}Y_{10}$) can be measured and quantified. Since then, this method has been used in a number of research to study atomic strains and stresses in MG under different load conditions [24–26]. For example, Shahabi et al. [24] tested *in situ* a plastically deformable Zr-based MG using SXTS. They found that, in the elastic regime and within the short range ordered (SRO) and medium range ordered (MRO) atomic structures, the atomic strains vary linearly with the applied macroscopic stresses. In the SRO structure, the atomic bonds were significantly stiffer than those in the MRO structures. Wang et al. [25] reported a dual-step atomic strain variation in a laser-shock-peened MG during an *in situ* SXTS experiment. So far, most SXTS studies have demonstrated that, in the SRO and MRO structures, local structure heterogeneity does exist [27–29], although in the long-range atomic distance MGs are often viewed as homogeneous materials. In a multiple-component system, the SRO structures are often characterized by the solute-centred atomic configuration. While the MRO structures can be constructed by linking or packing together the SRO structures [30,31]. During deformation, the SRO and MRO clusters or the different atom pairs in those clusters may respond differently to the external stresses. For example, Mattern et al. [32] measured the anisotropic responses of atomic structure in a Zr-Cu MG under uniaxial tension. They found that majority of the Zr-Zr pairs are reoriented towards the longitudinal direction, while at the same time, majority of the Cu-Zr pairs are reoriented towards the transverse direction. Liu et al. [33] studied atomic evolution of the MRO clusters in a $Pd_{82}Si_{18}$ binary MG under bending. They found that, in the tensile region, the connection of MRO clusters change from 2-atom sharing to 3-atom sharing configuration. While, in the compressive region, the changes occur in the opposite way. Until now, atomic evolutions in binary MG systems during deformation have been widely reported. However, there are very limited studies concerning any multicomponent MG system. How exactly the different atom species rearrange themselves in a 3D space to accommodate the local stresses/strains or to initiate shear bands has not been seen reported. The difficulty lies at how to construct accurate 3D atom models that agree with the measured total scattering data obtained at different load conditions, which is the basis for interrogating the relevant partial atomic pairs' movement at different stress conditions.

Recently, we have demonstrated that the Empirical Potential Structure Refinement (EPSR) method [34,35] is a very computationally-efficient method for constructing such a 3D model containing tens of thousands of atoms. Then, the partial distribution function for each atomic pair in a disordered alloy system can be systematically analysed [36–40]. Here, we report a well-executed complementary research of combining *in situ* SEM imaging and real-time SXTS together to study the stress-induced atom structure evolution/reconfiguration and the effect on shear band initiation in a commercial multicomponent Zr-based MG, $Zr_{41.2}Ti_{13.8}Cu_{12.5}Ni_{10}Be_{22.5}$. This alloy was chosen as the experimental alloy because it is the first commercially successful bulk MG with wider engineering applications [41] and several variants have been developed based on its composition [42]. Real-space images collected *in situ* inside an SEM allow us to "see" the onset and propagation of shear bands. Based on the X-ray total scattering data collected in the identical condition by SXTS experiment, we then used the EPSR method to model and reconstruct the 3D atomic structures at each measured stress step. Such rich and complementary real-time information allow us to understand fully how different atom pairs move, coordinate and rearrange themselves in 3D space in order to accommodate the tensile or compressive stress/strains, and which atomic pair is dominant in initiating shear bands. This research has demonstrated a powerful synergetic research methodology by effectively combining the complementary electron micrscopy and synchrtron X-ray technique together to realise, in operando conditions, multimodal and cross-length scale studies of materials. Such methodology can be explored widely in engineering materials with sample dimension from millimetre to centimetre range which are more representative than the micrometre or nanometre thin foil samples often used in the TEM observation or the FIB machined micro-pillar or micro-cantilever samples. It has wide applicaitons in accelerating the design, characterization and optimisation of new and existing multiple-component alloys from atomic level onwords.

2. Experimental methods

2.1. Alloy and samples

The alloy used in this study ($Zr_{41.2}Ti_{13.8}Cu_{12.5}Ni_{10}Be_{22.5}$) was made by melting pure Zr, Ti, Cu, Ni and Be elemental button ingots (each with purity >99.9 %, and weight ratio according to the designed composition) in an arc remelting furnace with Ti-gettered argon atmosphere [21]. The button ingots were electrical-discharging machined into dog-bone shaped tensile microtest samples with a notch in the middle along one edge of the gauge length (see Fig. 1a). The details of alloy and sample making are described in the Supplementary Materials (section 1.1).

2.2. In situ micromechanical tensile test inside SEM

The micromechanical tensile tests were carried out using a Deben 2000 Microtest with 2 kN load cell inside a Zeiss Evo 60 environmental SEM operated at 20 kV. The SEM is housed at the Electron Microscopy Centre of the Faculty of Science and Engineering, University of Hull. The recorded load-displacement curve is shown in Fig. 1b (the black line) (see section 1.2 of the Supplementary Materials). The fracture strength and strain are ~2032 MPa and ~2.4 % respectively (Fig. 1b), close to the reported tensile strength (1.9 GPa) and strain (2.0 %) [42] for this type of alloy. The fitted tensile stress-strain relationship based on the data indicated by the green squares shows a linear relationship and it is in the elastic region (the green line in Fig. 1b).

2.3. In situ SXTS experiments

The SXTS experiments were carried out at the Joint Engineering, Environmental and Processing beamline (I12) of Diamond Light Source (DLS) [43]. The identical tensile load conditions were applied using the same Deben 2000 Microtest. However, the dog-bone sample clamp arrangement was modified to avoid any blocking of the diffracted X-rays onto the detector as illustrated in Fig. S1 of the Supplementary Materials. The schematic experimental setup is shown in Fig. S1 in the Supplementary Materials (section 1.3). The load-displacement curve

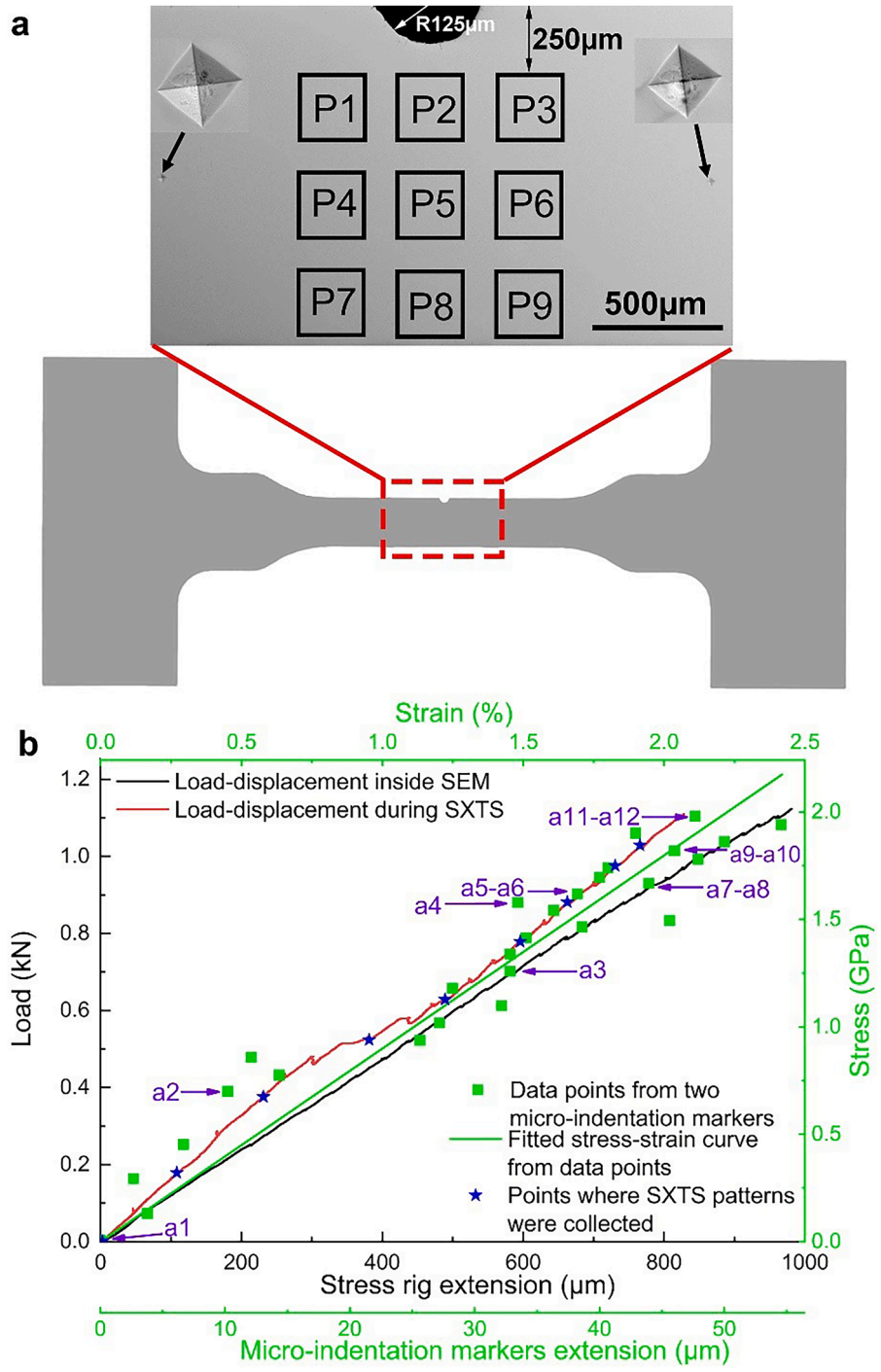

Fig. 1. The sample geometry and the stress-strain curves obtained in the *in situ* tensile tests. (a) A CAD drawing, showing the dog-bone shaped sample and dimension (23.72 mm long, 1.5 mm wide and 0.5 mm thick) with an SEM image inset, showing the semi-circular notch (250 μm in diameter) machined at the middle of the top edge of the gauge length. Nine squares (each of 250 × 250 μm^2) marked by P1, P2, …, P9 below the notch are the areas where SXTS patterns were collected. P2 is 125 μm below the notch. Two micro-indentations (pointed by the two black arrows and also enlarged on the insert) were also made at a distance of 2255 μm apart as markers for measuring *in situ* the sample extension at different load steps. (b) The load-displacement curves recorded by the Deben 2000 microtester inside the SEM (the black line) and in the SXTS experiment (the red line). The blue star markers show the load levels where the SXTS patterns were collected, and green square markers show the extensions between the two micro-indentation markers and the calculated strains. The green line is the fitted stress-strain relationship based on the data from the green square markers. The purple arrows point the stresses showed on the SEM images of Fig. 3.

recorded by the microtester (the red curve in Fig. 1b) has very similar slope compared to the one recorded in the SEM case (the black curve in Fig. 1b). The sample fractured at ~1968 MPa, about 3 % lower than that in the SEM case (2032 MPa), well within the measurement error range.

2.4. Data processing

To calculate the strain anisotropy in different azimuthal angle regions, each SXTS pattern was divided into 36 sectors. Each with 10° and its angle centre partitioning line represents the sector direction. Then integration was made in the 10° sector to produce the corresponding *I*(*Q*,

φ) or $I(2\theta, \varphi)$ spectra for that sector. For example, for the $\varphi = 0°$ direction, the integration was made from $-5°$ to $5°$. For the $\varphi = 180°$ direction, it was integrated from $175°$ to $185°$ (see the red lines in Fig. 2a). The integrations were made using DAWN 2.11 [44]. Then the structure factor, $F(Q, \varphi)$, and the reduced PDF, $G(r, \varphi)$, were calculated using the GudrunX [45]. The procedures for data processing are detailed in section 1.4 of the Supplementary Materials.

2.5. EPSR modelling

The EPSR method (version 25) [35] was used to simulate and reconstruct the 3D atomic model as well as extract the partial atomic pair information from the reduced PDFs. The detailed procedures are as below. Firstly, a total of 5000 atoms (Zr: 2060 atoms, Ti: 690 atoms, Cu: 625 atoms, Ni: 500 atoms, and Be: 1125 atoms) were chosen in a simulation box with the edge length of 43.40 Å. Secondly, the $F(Q)$, calculated by GudrunX was input into the model, and the weight factors were calculated accordingly (see section 1.4 of the Supplementary Materials). Thirdly, the EPSR input files with the default settings was created based on the five atom species, simulation box size and weight factors. Tests show that the default settings of the EPSR model works well for the simulations in this research. The periodic boundary

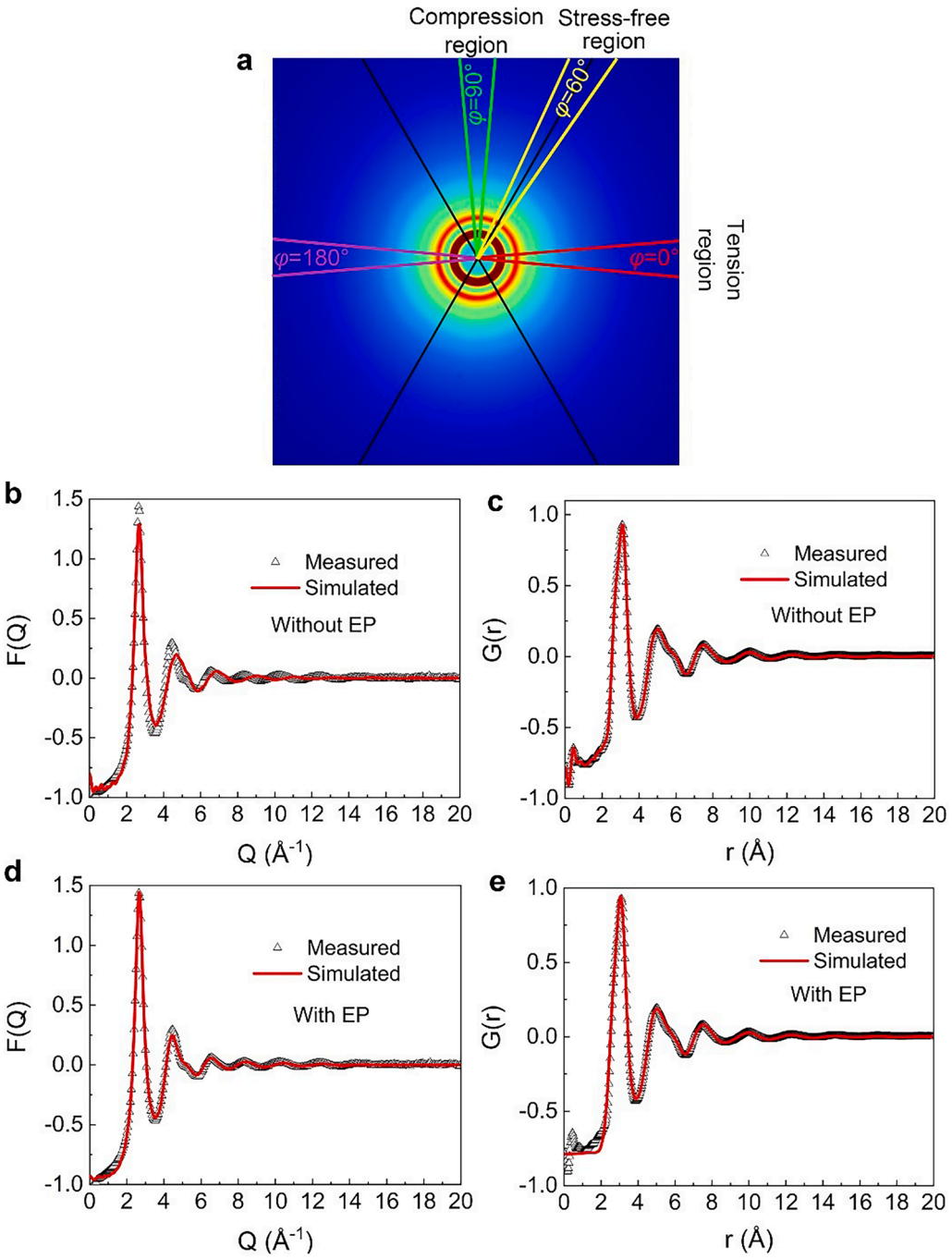

Fig. 2. Partition of the different azimuthal angle regions in a typical 2D total scattering pattern, and the F(Q) and G(r) for the EPSR modelling. (a) A typical 2D total scattering pattern and four azimuthal angular regions (sectors) along the direction of $\varphi = 0°$ (tensile stress), $\varphi = 60°$ (zero stress), $\varphi = 90°$ (compressive stress) and $\varphi = 180°$ (tensile stress) respectively; (b) and (c) the F(Q) and G(r) without empirical potential (EP) applied. (d) and (e) the F(Q) and G(r) with the EP applied. Note that the scattering data used in Fig. 2(b-e) was integrated along both $\varphi = 0°$ and $\varphi = 180°$ direction and then averaged.

condition was applied in the structure model.

A Lennard-Jones type reference potential with the parameters [35] listed in Table S2 was used first to drive the movement of the atoms (i.e., without applying the empirical potential). Fig. 2b and c show that, when only the reference potential was used, there were large discrepancies between the simulated $F(Q)$, $G(r)$ and the measured $F(Q)$, $G(r)$. A systematic test and optimisation indicated that, when an empirical potential (9 kJ/mol) was introduced in the model, the simulated $F(Q)$ agreed well with the measured one (compared Fig. 2b with d), except in the Q-range below 1 $Å^{-1}$ (Fig. 2d). This is due to two issues. First, it is very difficult to obtain accurate scattering data in the large scattering angle range [46]. Second, it may be due to the finite size of the simulation box [47]. The simulated $G(r)$ also matched the experimental data very well (see Fig. 2e). To compare the simulated $F(Q)$s and $G(r)$s in other stress states, Fig. S2 show all the simulation results in three stress states at different stress levels. For comparison, the experimentally measured ones were also plotted. For this 5-element amorphous alloy, our research demonstrated that the EPSR modelling is able to produce the simulation results that match the measured total scattering data perfectly. From the simulated 3D atomic structures, the 15 partial PDFs (see the example in Fig. S3 of the Supplementary Materials), bond angle distributions were extracted for further analyses. To calculate the bond angle distributions of linkages, the distances of each atomic pair used in this work are listed in Table S3, which are the upper limits of the bond length of each atomic pair in the 1st atomic shell. The EPSR simulation was performed using one of the dedicated computing nodes (2 × 14-core Broadwell E5–2680v4 processors (2.4 - 3.3 GHz), 128 GB DDR4 RAM) of University of Hull supercomputing cluster, Viper. It normally takes approximately 6 h computing time (~2000 iterations) to complete a typical simulation with a satisfactory R-factor (an indication of the difference between the simulated and the experimental $F(Q)$) of 10^{-3}. To ensure reproducibility and increase statistics, the EPSR simulation was repeated 3 times for each SXTS pattern of the sample acquired at each stress level. The results presented in this paper are the averaged results of those simulations.

3. Results

3.1. Results of in situ SEM imaging study

The initiation and subsequent propagation of shear bands of the Zr-based MG dog-bone samples were observed *in situ* by SEM (Fig. 3, see Video 1 and Video 2 for the dynamic information more clearly). The corresponding tensile stresses are plotted in Fig. 1b (marked by the purple arrows). There were two small pre-existing cracks at the notch edge due to electric discharging machining (Fig. 3a1), and such cracks were able to facilitate the initiation of shear bands due to their additional stress concentration effect on top of that generated by the semi-circular notch.

When the tensile stress was increased to 699 MPa, very fine shear bands were observed at the tips of the pre-existing cracks (the inset in Fig. 3a2). When the tensile stress reached 1263 MPa (Fig. 3a3), a number of shear bands grew up to 20 ~ 30 μm long. When the tensile stress reached 1549 MPa, the length of shear bands increased remarkably, especially near the right crack (about 100 μm). The shear bands opened up to become cracks (Fig. 3a4). The growth direction of most shear bands was perpendicular to the tensile loading direction. On a further increment of the tensile stress to 1585 MPa, a shear band pointed by A (Figs. 3a and 5) grew much faster than the other shear bands and propagated into the square region marked by P2 (Figs. 5 and 3a), indicating that the shear band arrived at P2 at around 1585 MPa.

Most shear bands propagated through P2, while just one shear band was seen to touch on the left edge of P3 (see Video 1). Hence, we focused on studying the shear bands passing through P2 as shown in Fig. 3. Three other shear bands marked by B, C, and D respectively propagated into P2 when the tensile stress reached 1676 MPa (Fig. 3a7, a8). Upon further increasing the tensile stress to 1829 MPa and 1991 MPa (Fig. 3a9–a12), the shear bands passing through P2 gradually developed into full-fledged cracks. Finally, those cracks propagated through P2, and fractured the sample at 2032 MPa (Fig. 1b). Video 1 and 2 show more clearly

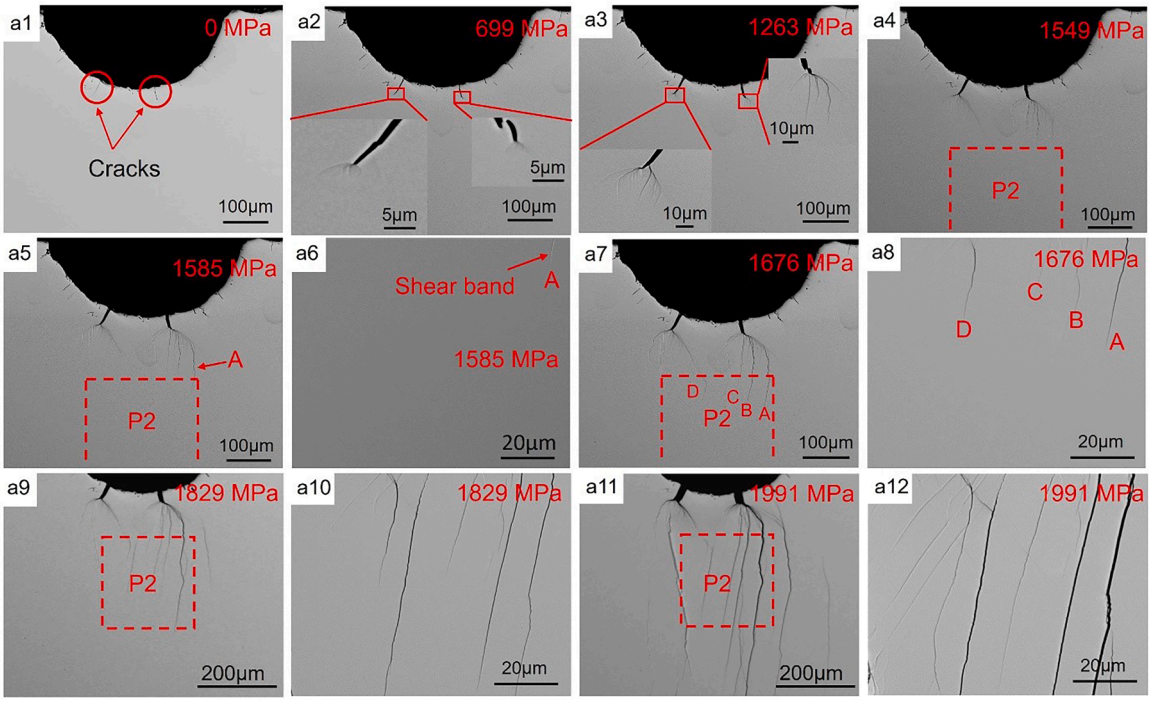

Fig. 3. The initiation and propagation of shear bands observed *in situ* by SEM. a1–a5, a7, a9 and a11 are the SEM images near the notch of the dog-bone sample captured at tensile stresses of 0, 699, 1263, 1549, 1585, 1676, 1829 and 1991 MPa, respectively, showing the initiation and propagation of shear bands under different tensile stresses. a6, a8, a10 and a12 are the enlarged images of shear bands/cracks at location P2 in (a5), (a7), (a9) and (a11) respectively, highlighting the propagation of shear bands and the formation of full-fledged cracks in the region of interest, i.e., P2. See Video 1 and Video 2 for the dynamic information more clearly. Note: the stresses are applied along the horizontal direction.

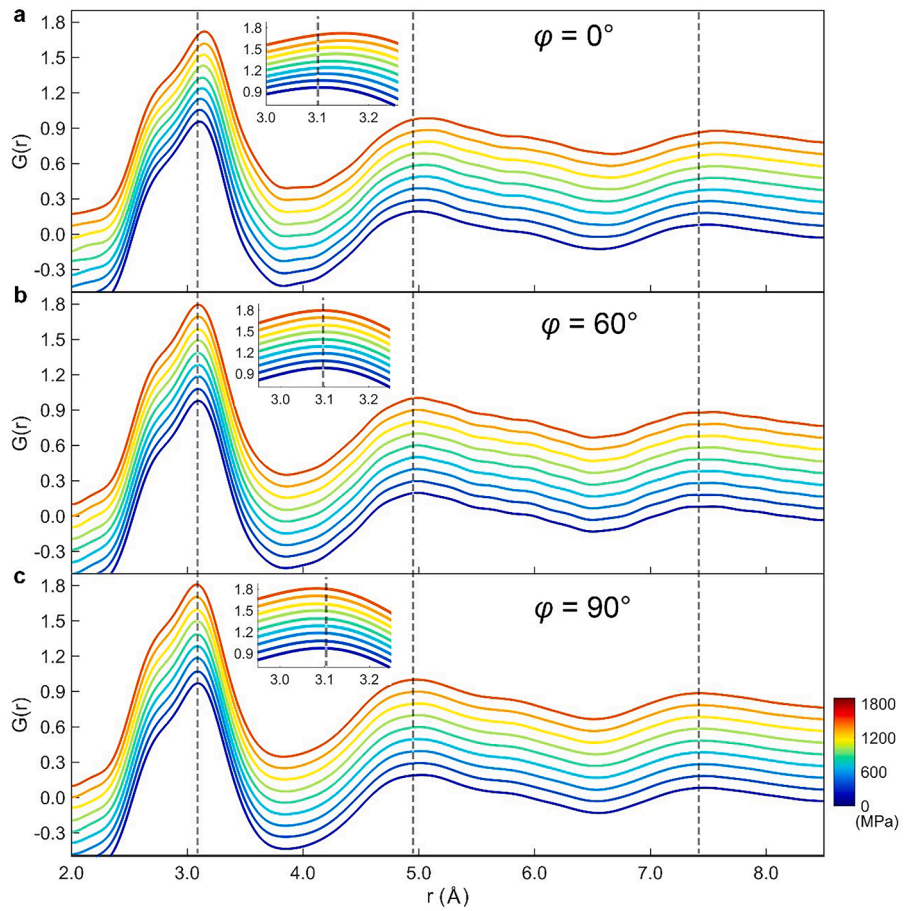

Fig. 4. The G(r)s in different angular sectors at different levels of tensile stresses. (a) along φ = 0°, (b) φ = 60°, and (c) φ = 90° direction respectively. The G(r)s are stacked together with an equal offset spacing of 0.1 in y axis; only data for the range of 2 Å < *r* < 8.5 Å are shown here to highlight the position shifts of the 1st, 2nd and 3rd peaks. The dashed lines mark the peak positions of the unstressed sample.

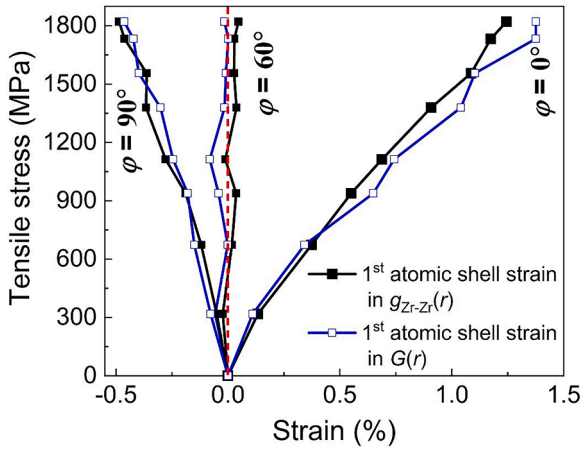

Fig. 5. The atomic strains calculated from the peak shifts of the 1st atomic shell in G(r) and $g_{Zr\text{-}Zr}$(r)s along φ = 0°, φ = 60° and (c) φ = 90° direction respectively.

the dynamic propagation behavior of these shear bands.

3.2. Results of in situ SXTS study

The SXTS patterns were collected at nine square locations (marked by P1-P9 in Fig. 1a insert). Because most shear bands propagated through P2 (see Video 1 and Video 2), only the data collected at location P2 are reported in this paper.

For each 2D SXTS pattern obtained at each stress step, the strain in each of the 10° sectors of that pattern was calculated based on the position shifts of the 1st peak of the *I*(*Q*) curves (see Section 2.1 of the Supplementary Materials). The peak positions were found and determined by Gaussian fitting of the *I*(*Q*) curves. The calculated strain contour maps are presented in Fig. S4a. It clearly shows that, in the angular range of 0° < *φ* < 60° and 120° < *φ* < 180°, positive strains were developed as the applied stress increased, while along *φ* = 60° and *φ* = 120° directions, the strains were approximately zero. In the *φ* range of 60° < *φ* < 120°, negative strains were developed with the increase of the applied stress. Hence, the maximum positive strain (i.e., maximum tensile stress) was along *φ* = 0° direction (the longitudinal direction); while the maximum negative strain (i.e., maximum compressive stress) was along *φ* = 90° direction (the transverse direction). Stress-free state existed along *φ* = 60° and *φ* = 120° directions, as marked by the two black lines in Fig. 2a. Fig. S5 also shows the *I*(*Q*) curves along *φ* = 0°, 60° and 90° direction respectively. The 1st peak position shifted towards the low *Q* value along *φ* = 0° direction (see the inset in Fig. S5a), but moved towards the high *Q* value along *φ* = 90° direction (see the inset in Fig. S5c). While the 1st peak position remained unchanged along *φ* = 60° direction (see the inset in Fig. S5b). Based on each *I*(*Q*), the PDFs were calculated and shown in Fig. 4. Clearly, the 1st peak position of *G*(*r*)s shifted towards the higher *r* along *φ* = 0°, but lower *r* along 90° direction (inset in Fig. 4a, c), while no changes along *φ* = 60° direction (inset in Fig. 4b). The position shifts of the 1st, 2nd, and 3rd peaks of the PDFs at each stress step were also used to calculate the atomic shell strains in real space (see Section 2.1 of the Supplementary Materials).

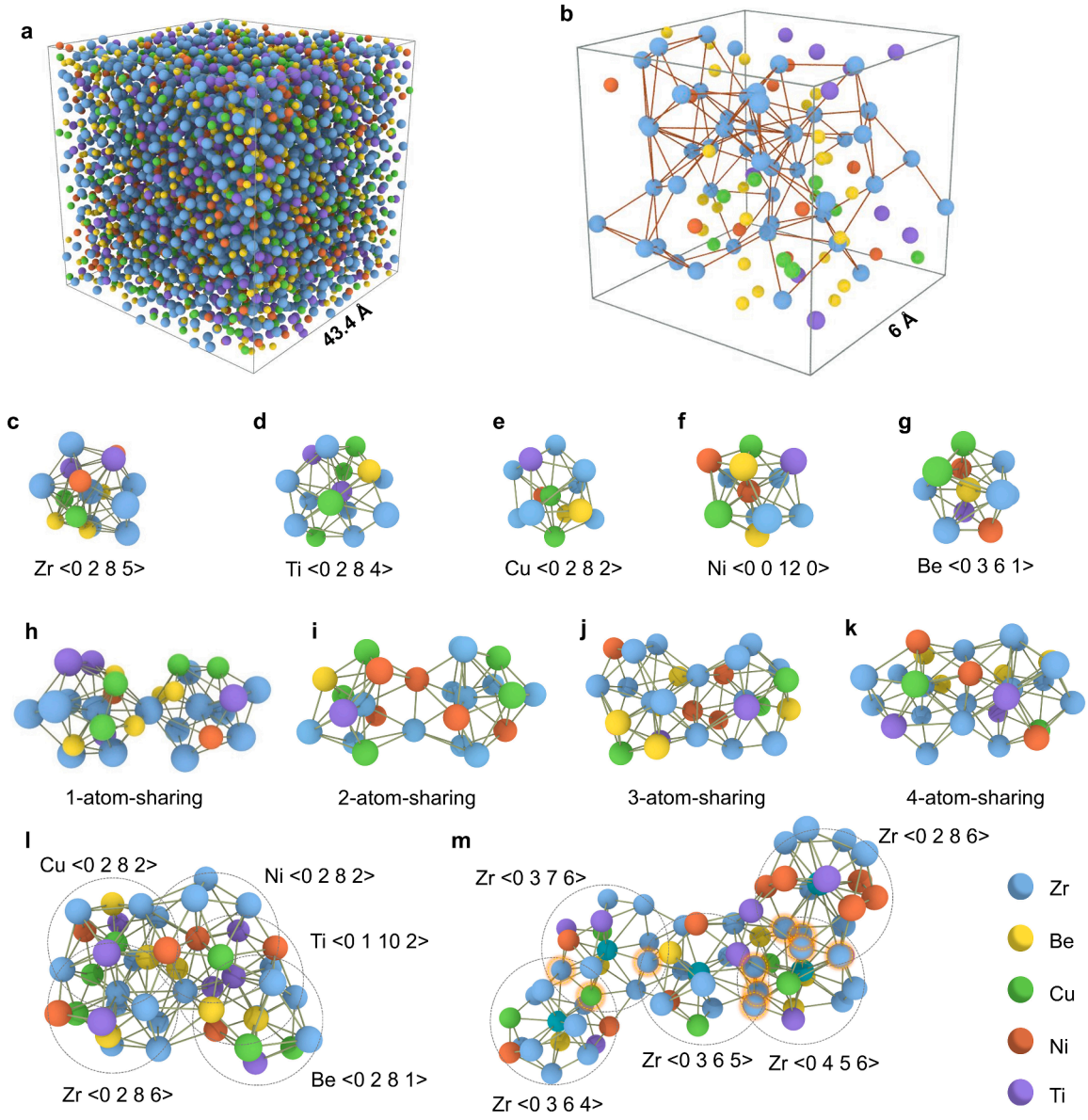

Fig. 6. The 3D atomic structure of the Zr-based multicomponent MG extracted from the EPSR simulation results. (a) All atoms in the box are at zero stress along φ = 0° direction; (b) A typical small volume within the simulaiton box, showing the Zr-Zr bonds and the surrounding atoms; (c-g) Typical SRO structures with the Zr, Ti, Cu, Ni and Be as the centre-reference atom respectively; (h–k) Typical MRO structures formed by sharing 1, 2, 3 and 4 atoms respectively (only the Zr-centred clusters are presented here); (l) A supercluster formed by connecting the Zr-centred, Ti-centred, Cu-centred, Ni-centred and Be-centred SRO clusters; (m) Another supercluster formed by different connection modes of Zr-centred SROs with the shared atoms highlighted by shadows. Video 3 shows, in 3D, more vividly the SROs, MROs and the superclusters formed by connecting the SROs and MROs via different connection modes.

Fig. S4b-d shows the calculated atomic strains contour maps for the 1st, 2nd, and 3rd atomic shells. Apparently, they exhibited the same characteristics as those calculated from the *I(Q)* curves, i.e., the deformation anisotropy exists in different φ angels.

Fig. 5 shows the strains calculated from the 1st peaks of $G(r)$s along φ = 0°, 60° and 90° directions respectively. For comparison, the strains calculated from the 1st peak shift of the $g_{Zr\text{-}Zr}(r)$s (the partial PDFs extracted from the EPSR modelling results as explained below) are also plotted in Fig. 5. Interestingly, the atomic shell strains calculated by the two methods are almost identical under the same applied stresses.

3.3. Results of the EPSR modelling

3.3.1. Partial PDFs of the 15 atomic pairs and their evolutions with different stresses

At each applied stress, the EPSR modelling was executed to obtain the $G(r)$ that matched the total scattering data and then reconstruct the 3D atomic structures. The results of the *ab initio* molecular dynamics calculations from [48] were also referenced here for comparison with the EPSR results (see Section 2.2 in the Supplementary Materials and Table S4). Fig. 6a shows, at zero stress, the 3D atom structures modelled by the EPSR (5000 atoms). Video 3 illustrates more vividly the 3D atom configurations when zooming into a small volume showing the Zr-Zr bonds and the surrounding atoms, as well as the typical SROs, MROs and superclusters.

To show more clearly the Zr-Zr bonds and the surrounding solute

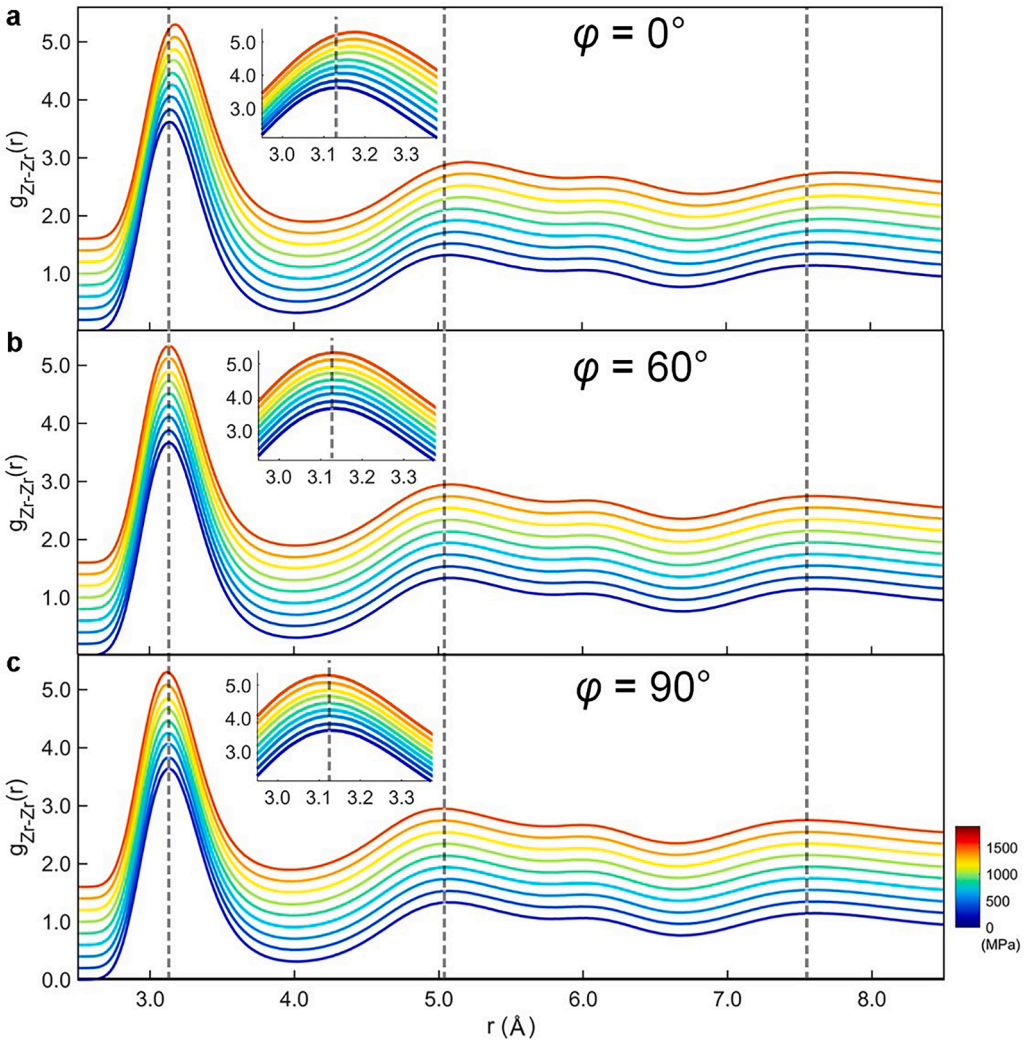

Fig. 7. The $g_{Zr\text{-}Zr}(r)$s extracted in different azimuthal angles exrected from the EPSR models at different stress levels. (a) along φ = 0°, (b) φ = 60°, and (c) φ = 90° direction respectively.

atoms, Fig. 6b shows a small volume with the edge length of 6 Å and only the bonds of Zr-Zr pairs are presented. From the EPSR model, for any arbitrary reference atom, its nearest neighbour atoms (i.e., the 1st coordination shell atoms) can be extracted as shown in Fig. 6c–g when using the Zr, Ti, Cu, Ni and Be as the centre-reference atom. These 1st coordination shell atom clusters are the building blocks for constructing the MRO structures via different linkages as clearly indicated in Fig. 6h–k. Furthermore, Fig. 6l and m illustrate respectively two typical super atomic clusters which are built by grouping these SRO structures in a more complicated way. Readers are recommended to view Video 3 so as to appriciate more deeply the 3D strucutres of the SROs, MROs and the superclusters formed by connecting the SROs and MROs via different connection modes.

The partial PDF and bond length of any atomic pair at each stress step were also extracted from the 3D model. Fig. 7 shows the extracted partial PDFs of $g_{Zr\text{-}Zr}(r)$s along $\varphi = 0°$, 60° and 90° directions respectively. The peak positions shifted toward higher r along $\varphi = 0°$ direction and lower r along $\varphi = 90°$ direction (see the inset in Fig. 7a and c). While no obvious change of the peak positions along $\varphi = 60°$ direction (the inset in Fig. 7b). Fig. 8a and b show the bond length of the 15 partial PDFs and their relative changes along $\varphi = 0°$ direction respectively (see Fig. S6a and S6b for the bond length data along the $\varphi = 60°$ and 90° direction as well). Fig. 8b shows that, the bond length of the Zr-Zr atomic pair increased linearly with the increase of tensile stress (a total of ~1.24 %). It reached its theoretical value of 3.16 Å [49] at ~1113 MPa (see the inset in Fig. 8a). Bond lengths of the Zr-Cu, Zr-Ni, Zr-Ti pairs remained relatively unchanged. While that of the other 11 atomic pairs decreased in the range of −0.38 % – −0.66 % (Fig. 8b). By contrast, along $\varphi = 90°$ direction (see Fig. 8d and Fig. S6b), only bond length of the Zr-Zr pair decreased monotonously (−0.49 %), those of other pairs remained unchanged (Fig. 8d) or just slightly changed. Along $\varphi = 60°$ direction, the bond lengths of all pairs remained unchanged (see Fig. S6a and Fig. 8c). Along three azimuthal angle directions, the strains obtained from the shift of the 1st peak position of $G(r)$s were almost identical to the relative change in bond length of the Zr-Zr pair (Fig. 5).

3.3.2. *Bond angle distributions and their evolutions with different stresses*

Fig. 9a and b show the typical bond angle distributions of Zr-Be-Zr linkage at different stresses along $\varphi = 0°$ and $\varphi = 90°$ direction respectively. As the tensile stress increased, the peak positions of Zr-Be-Zr linkage increased monotonously along $\varphi = 0°$ direction, while those decreased gradually along $\varphi = 90°$ direction. The similar trends were observed in the Zr-S-Zr linkages (S denotes the solute atoms, i.e., Ti, Cu, Ni and Be, see Fig. S7 and Fig. S8). Fig. 9c and d show the bond angle distribution of Be-Zr-Be linkage, and its peak positions moved towards lower angle along $\varphi = 0°$ direction, but towards higher angle along $\varphi = 90°$ direction. The peak positions of Ti-Zr-Ti, Cu-Zr-Cu and Ni-Zr-Ni linkages show the similar trend as that of Be-Zr-Be linkage (see Fig. S9

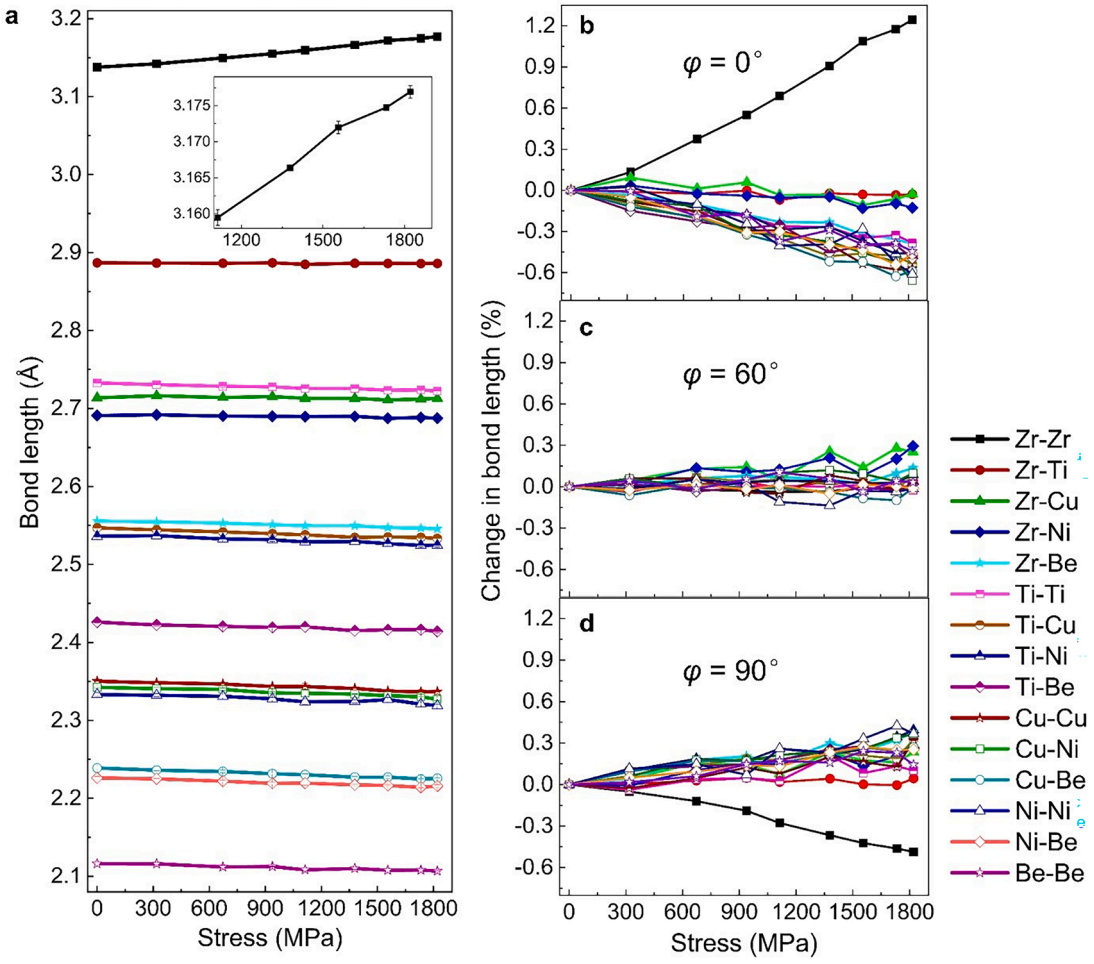

Fig. 8. (a) Changes of bond length of all 15 atom pairs versus stress along φ = 0° direction, and the relative change along (b) φ = 0°, (c) φ = 60° and (d) φ = 90° direction respectively.

and Fig. S10). Fig. 9e shows the relative shift of the 1st peak in the different Zr-S-Zr and S-Zr-S linkages. The 1st peak positions of the Zr-S-Zr linkage increased almost linearly with stress increasing. The Zr-Be-Zr linkage showed the highest percentage of increasing (~1.71 %), while the Zr-Cu-Zr linkage was the lowest in percentage of increasing. Both Zr-Ti-Zr and Zr-Ni-Zr linkages showed similar and moderate percentage increase (Fig. 9e). To understand how other four solute atoms maneuver around the Zr atom under an increased stress, the relative changes in bond angles of the S-Zr-S linkages along $\varphi = 0^\circ$ direction versus stress are also plotted in Fig. 9e. Clearly, not only the bond lengths of these atomic pairs (i.e., Ti-Ti, Cu-Cu, Ni-Ni and Be-Be showed in Fig. 8a, b) decreased, but all their bond angles (Ti-Zr-Ti, Cu-Zr-Cu, Ni-Zr-Ni, Be-Zr-Be) decreased monotonously as the stress increased. The percentage of decrease was in the range of 0.71 %–2.19 %. By contrast, there was an opposite trend in the bond angle of different linkages along $\varphi = 90^\circ$ direction (Fig. 9g), i.e., peak positions of the Zr-S pairs decreased and those of S-Zr-S linkages increased linearly. For the sample along $\varphi = 60^\circ$ direction (Fig. 9f), the bond angles of all linkages slightly oscillated around zero. The similar trends were also found for the 2nd peak position (not shown here). To further understand how the solute atoms move in response to the increased stress, the percentage of changes in bond angles between solute only atoms (S-S'-S, i.e., the Zr atom is excluded) are plotted in Fig. S11. Interestingly, the general trends are quite random along all three directions.

3.3.3. Voronoi tessellation analysis and bond-orientational order

Fig. S12a shows that, along $\varphi = 0^\circ$ direction, as the applied stress increases from 0 MPa to 1821 MPa, the average CN for the Zr atom increased monotonously by 1.3 % from 13.35 to 13.53. However, the CN for all other atoms did not show any clear trend. Along $\varphi = 90^\circ$ direction (Fig. S12c), the trends for CNs are in opposite direction, i.e., CN for the Zr atom decreases from 13.35 at 0 MPa to 13.26 at 1821 MPa (decreased by 0.7 %). Again, the CNs for the other atoms remains unchanged (Fig. S12c). Apparently, along $\varphi = 60^\circ$ direction, there is no obvious change for all CNs (Fig. S12b). Fig. S12d–f shows the changes of $\widehat{W}_6$ versus the applied stress along the three directions (see Section 2.3 of Supplementary Materials). Clearly, the $\widehat{W}_6$ of Zr is the highest and in the range of −0.03348 to −0.0319. It has been reported that the $\widehat{W}_6$ for the icosahedral-type atom clusters with the CN of 12 is −0.170 [50,51]. Further, the CN for the Zr atom is over 13 and therefore, the Zr-centred clusters have a lower degree of icosahedra, often called "fragmented polyhedra" [52]. While the CNs for other solute atoms (S-centred clusters) are around 12 and the their $\widehat{W}_6$ values are approaching to those of the icosahedral-type atom clusters, indicating that S-centred clusters can be considered as "icosahedral-like clusters" with a higher degree of icosahedra [52]. The typical supercluster formed by linking together the (Zr, Ti, Cu, Ni, Be)-centred clusters support this argument (see Fig. 6l).

3.3.4. MRO structures and their connection modes

MRO structures are those beyond the 1st atomic shell (i.e., beyond the 1st peak of $g(r)$) and they can be viewed as being constructed by connecting the SRO structures *via* 4 different connection modes (see Fig. 6h-k, by sharing 1, 2, 3 or 4 atoms [53–55]). As indicated in Figs. 8,

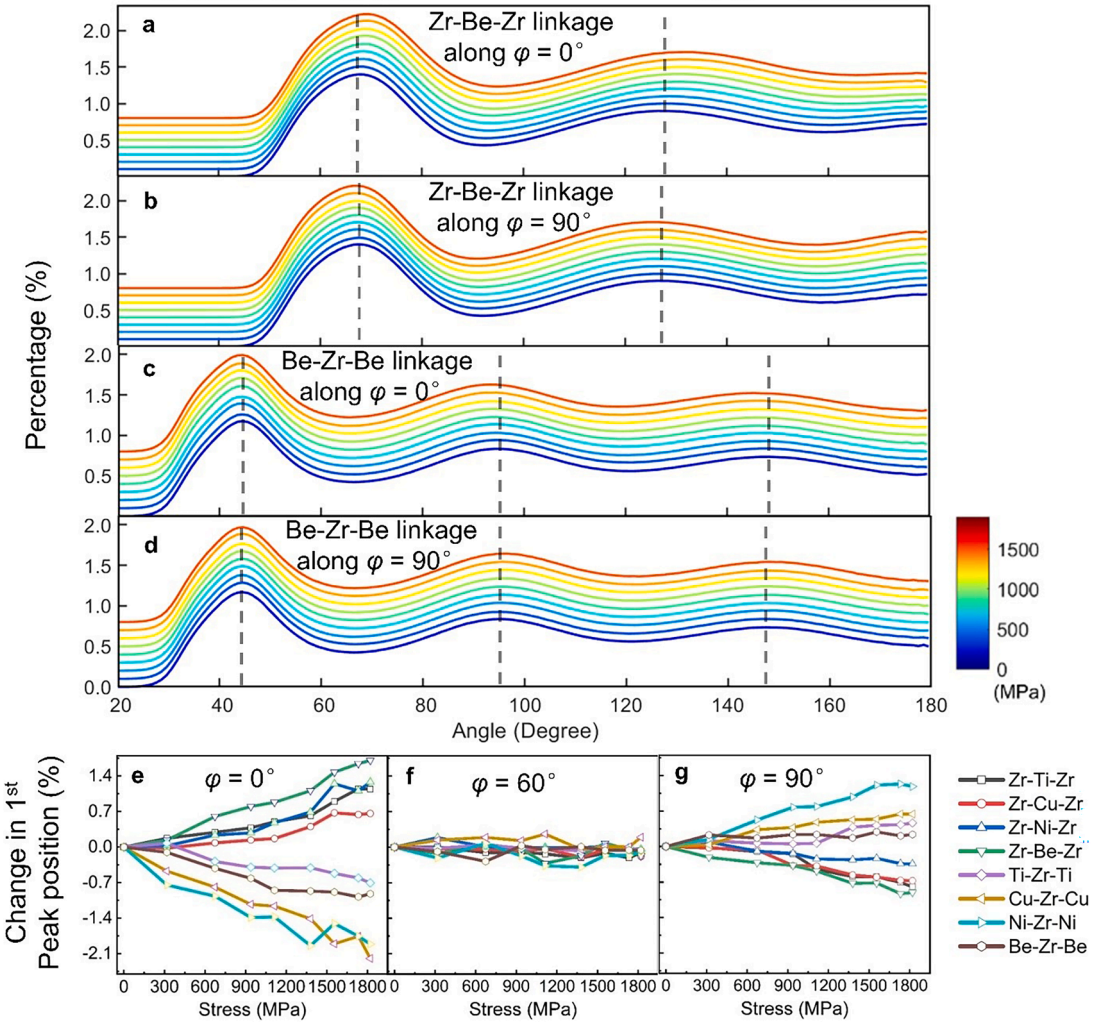

Fig. 9. Bond angle distributions extracted from the EPSR models and their relative changes versus stress. (a) and (b) for Zr-Be-Zr linkage along φ = 0° and φ = 90° direction respectively; (c) and (d) for Be-Zr-Be linkage along φ = 0° and φ = 90° direction respectively; (e)-(g) Relative changes in bond angles of Zr-S-Zr and S-Zr-S linkages along φ = 0°, φ = 60° and φ = 90° direction respectively.

9 and S12, the Zr-centred clusters played the dominant role in atom evolution during deformation. Hence, we focused on interrogating the Zr-centred clusters further.

Fig. 6m shows an example of an MRO cluster consisting of all 4 connection modes. Fig. 10a–d show percentage changes of the 4 connection modes versus stress along the three directions respectively. Clearly, along $\varphi = 0°$ direction, the 1-atom-sharing connection decreased monotonously versus stress. The 2-atom-sharing connection and 3-atom-sharing connection increased gradually, while the 4-atom-sharing connection showed a bit less increasing (see the black lines in Fig. 10a–d). By contrast, along $\varphi = 90°$ direction, the 1-atom-sharing connection increased slightly and the 4-atom-sharing connection decreased rapidly with stress. While 2-atom-sharing and 3-atom-sharing connection remained virtually unchanged (see the green lines in Fig. 10a-d). There are no changes along $\varphi = 60°$ direction for all connections.

4. Discussion

4.1. The advantage of the EPSR versus other methods for modelling and reconstructing 3D atomic structures for disordered alloy systems

For any multicomponent alloy, it is essential to obtain the partial PDFs of each atomic pair in order to understand precisely how different atoms rearrange themselves to coordinate the deformation. Currently, first-principle density functional theory (DFT) and *ab initio* molecular dynamics (AIMD) methods [56,57] are used to calculate the atomic configuration of binary or ternary metallic glasses or high-entropy alloys. However, the DFT method is difficult to deal with a system containing five or more elements, and AIMD method is limited to small systems (normally a few hundred atoms) and a short period of time (~10–100 ps) [58]. Furthermore, although classical Gaussian fitting technique [59] and reverse Monte Carlo fitting method [60] are often used to decouple the partial PDFs with large systems (several thousand atoms), the two methods do not have the physical meaning [61] and always run into difficulties when attempt to decouple all partial PDFs in multicomponent alloys. In this work, the EPSR method was used to compute and decouple all 15 partial PDFs in this 5-element metallic glass based on the experimentally collected SXTS data. It has been proven as a computationally efficient method for simulating disordered systems of many thousands of atoms [36–40]. In EPSR modelling, the Lennard-Jones potentials plus Coulomb charge interactions act as a starting reference potential, which captures the fact that atoms are not hard spheres and can be squashed up against each other (the r^{12} part of the potential). In longer range, the induction forces that come from the correlated motion of the electrons in the system (the r^6 part of the potential). These potentials are the simple background interactions that allows the EPSR refinement to proceed, i.e., to move the position of the

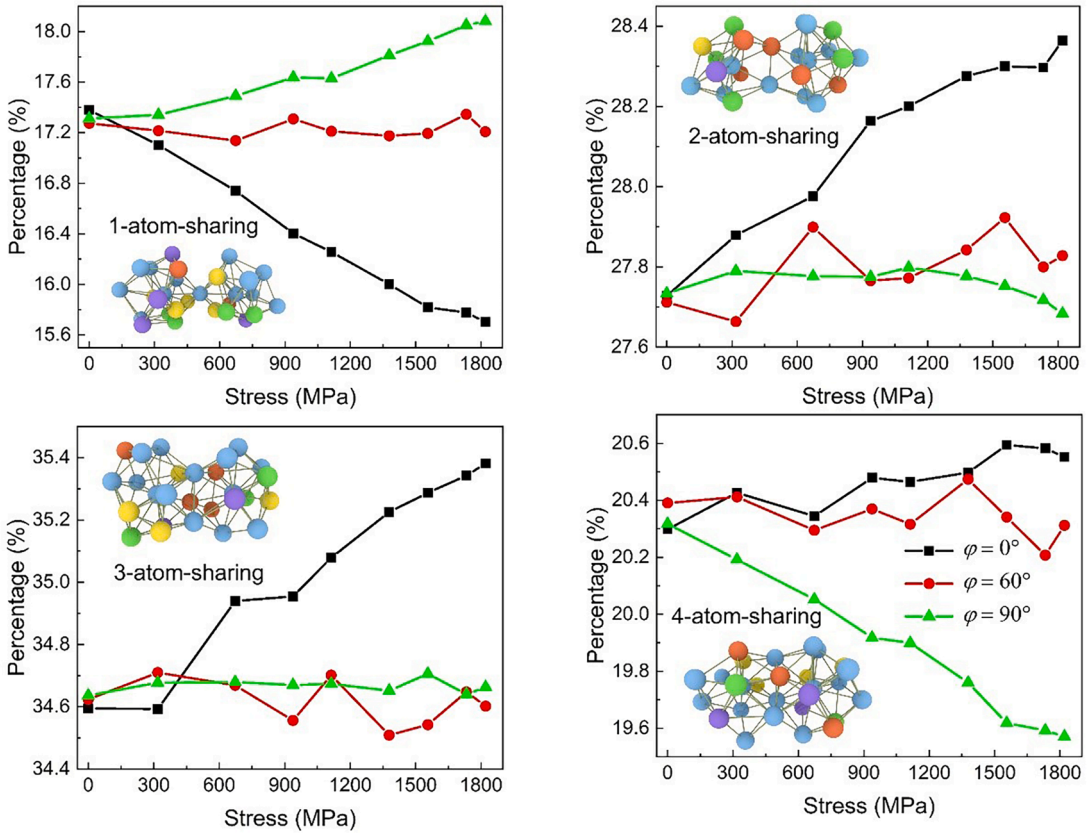

Fig. 10. Stress-induced atomic evolution of the Zr-centred MRO clusters along the three different directions. The 4 different connection modes are (a) 1-atom-sharing, (b) 2-atom-sharing, (3) 3-atom-sharing, and (d) 4-atom-sharing.

atoms in 3D space under a fixed bulk density of the system. On top of this, the empirical potential is then added as a perturbative force to capture the corrections that are required to put the positions of the atoms into agreement with the experimentally determined atomic pair distribution functions through the distance-dependent modifications to the interaction potentials. The EPSR simply aims to put the nuclear centres of the model atoms into positions consistent with the interpretation of neutron or X-ray scattering theory, one of the best understood and physically robust experimental tests that has been derived by modern science. In this work, the EPSR method can simulate the X-ray scattering data perfectly in both reciprocal and real spaces (Fig. 2d, e). Then all 15 partial PDFs can be extracted from the atomic structure model (Fig. S3). More importantly, the results obtained from the EPSR modelling are in good agreement with those calculated by AIMD method for this multicomponent metallic glass [48]. The bond lengths of different atomic pairs obtained from the EPSR method are very close to those obtained from the AIMD method (Table S4). Moreover, the Voronoi tessellation analysis results show that there is no dominant Voronoi polyhedra in this alloy although <0, 3, 6, 3>, <0, 3, 6, 4>, <0, 2, 8, 1> and <0, 2, 8, 2> VPs have a bit higher percentage than other VPs (Fig. S13). These are again similar to the results obtained from the AIMD method for this alloy [48]. The above results and comparison confirm that the EPSR method is a robust and computational efficiency technique for the simulation and reconstruction of the 3D atomic structure of multicomponent metallic glassy alloys.

4.2. The dominant atomic pair in governing elastic deformation and shear band initiation

Analogous to dislocations in crystalline materials, shear banding is the essential deformation mechanism in MGs [11]. A huge number of studies have been reported in investigating and characterising shear band initiation and propagation in different glassy alloy systems under different stress conditions (tensile, compressive, bending, shearing, etc.). The most common methods used are real-space image techniques, e.g., SEM and/or TEM or reciprocal diffraction technique, i.e., SXTS. *In situ* SEM and/or TEM observation can obtain images of shear bands at nanometre scale [13–17], but it is very difficult to obtain the local stress/strain information at the region close to the shear bands, especially difficult in obtaining such information at atomic level for a bulk sample of millimetre scale in an operando condition as in our case. In this aspect, *in situ* SXTS plus PDF analysis can provide stress/strain information at atomic scale from a bulk sample [24–26], however it cannot "see" directly where the shear bands are and how they propagate in the bulk sample. Hence, the link between shear band initiation/propagation and the local stress/strain ahead of the shear bands, especially at atomic level, has not been established. Recently, limited studies have been seen reported to use the combined approach of *in situ* electron microscopy imaging plus SXTS together and attempted to establish such link at atomic level [20–22]. Unfortunately, in those work, the partial PDF of each atomic pair was obtained by only estimating the weighting factor of each atomic bond, and the contributions of 7 atomic pairs were ignored in Zr-based multicomponent alloy [21]. In our work, by using the EPSR modelling to search and reconstruct the 3D structure model that matches the total scattering data at each stress level, we are able to decouple all 15 partial PDFs from the reduced PDF. Fig. 8a, b show clearly that, along $\varphi = 0°$ direction, with the increase of stress, the bond length of Zr-Zr atomic pair increases almost linearly, while the bond length of other atomic pairs remain almost unchanged or decrease by different degrees (Fig. 8b). Meanwhile, the Zr-S-Zr bond angles also increase monotonously with the stress (Fig. 9e). Such convincing evidence indicates that the extension of the bond length of Zr-Zr atomic pair and the continuous opening up of the Zr-S-Zr bond angles (both are in linear relationship with the applied stress) are the

main atomic structure changes in the alloy to accommodate the elastic strain. More interestingly, the strains obtained from the 1st atomic shell are almost identical to the change in bond length of the Zr-Zr pair (Fig. 5), indicating that the Zr-Zr pair plays the dominant role in controlling the elastic deformation of the 1st atomic shell as well in this multicomponent alloy. A simple schematic of how the atomic structure rearrange themselves in order to accommodate the extension of Zr-Zr bonds are illustrated in Fig. 11. At zero stress, a Zr-S-Zr angle is formed by two Zr atoms and one solute atom (referred to as ∠α), and a S-Zr-S angle is formed by two solute atoms and one Zr atom (referred to as ∠β). After applying the tensile stress, the two Zr atoms are extended further away from each other, i.e., the bond length is increased as indicated by the dashed blue lines. To accommodate the extension of Zr-Zr bond, the solute atoms move towards the Zr atoms, leading to decrease of bond length of the Zr-solute and solute-solute atom pairs and two new angles (∠α' and ∠β') are formed. Clearly, the ∠α' is larger than the ∠α, while ∠β' is less than the ∠β, consistent with the results showed in Figs. 8 and 9.

From the *in situ* SEM imaging study, a shear band is observed at ~1585 MPa (Fig. 3a5, a6). At the similar stress level (1556 MPa), the bond length of Zr-Zr pair in the longitudinal direction exceeds its theoretical value of 3.16 Å [49] (the inset in Fig. 8a), while the bond lengths of other atom pairs are below their corresponding theoretical values. When a metallic glass is subject to an external stress beyond its elastic limit, shear bands often initiate from the structural regions of relatively higher free volumes (i.e., the relatively soft regions) [62,63]. Dilation of these free volumes under further stresses can cause shear transformation and shear transformation zones [64]. The SRO and MRO clusters can therefore rearrange themselves to accommodate such shear dilation in the glass [65]. In this work, Zr-centred clusters have a lower degree of icosahedra (i.e., high free volumes), and therefore are more likely to be amenable and rearrange themselves during the initiation of shear bands. Hence, from statistics point of view, at the stress level that shear bands are seen to be initiated, there are higher probability of Zr-Zr bonds yielding or breaking, indicating that the yielding or breaking of Zr-Zr bonds indeed plays a critical role in the initiation of shear bands in this alloy.

4.3. SRO and MRO structure evolution in different stress states

The change or evolution of atomic structures at different stress conditions in MGs has been studied extensively [23,24,32,66]. The evolution of atomic clusters is closely linked to the stress states [32,67]. In the tested samples of this work, the tensile stresses are along the longitudinal direction ($\varphi = 0°$), while the compressive stresses are along the transverse direction ($\varphi = 90°$). In addition, almost no stresses are found along $\varphi = 60°$ direction (Figs. S4, S5). These give us perfect conditions to study how atomic structures rearrange themselves in different stress states.

As mentioned above, the Zr-centred clusters are fragmented

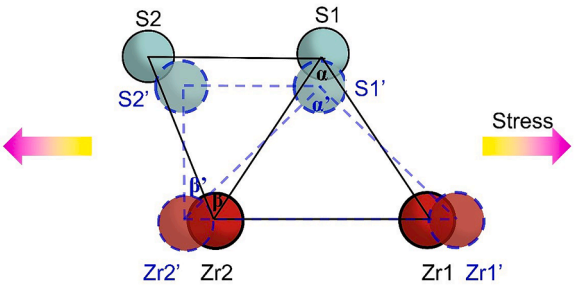

Fig. 11. A schematic of atomic structure evolution during the extension of Zr-Zr bonds. The solid black lines represent the atomic structure configuration at zero stress, and dashed blue lines represent the atomic structure configuration after applying stress. S represents the solute atom.

polyhedral clusters with low degree of icosahedra, while the S-centred clusters are icosahedral-like clusters with high degree of icosahedra. Many simulation studies [52,68,69] showed that, a cluster with higher degree of icosahedra has a higher atomic packing density (i.e., low level of free volume) and it is mechanically and energetically more stable (i.e., stiffer) than that with lower degree of icosahedra [70]. Our SXTS and EPSR modelling results clearly illustrate that the Zr-centred clusters have low degree of icosahedra and therefore they are preferred choices of atoms to make rearrangement in order to accommodate the deformation. The Zr-Zr pairs show the largest change in both tensile and compressive stress states, while other atom pairs show the opposite trends (Figs. 8 and S6).

Fig. 12 illustrates how the Zr-centred SRO and/or MRO clusters rearrange themselves in the different stress states. Fig. 12a shows that, before applying any stress, a typical MRO cluster with two Zr-centred clusters connected *via* the Zr-Zr bond. The Zr-X-Zr linkage (X represents the shared atom) forms the bond angle ∠ABC. In the tensile stress state and as it increases, the Zr-Zr bond length increases, "pulling" the surrounding X atoms to move towards the gap between the two Zr atoms. When the stress reaches the critical value, about 1379 MPa as revealed by EPSR modelling and *in situ* SEM imaging results, the Zr-Zr bond breaks and thus then the X atoms become the middle atoms that link the two Zr-centred clusters *via* 1, 2, 3 or 4-atom-sharing mode (Fig. 12b). In this scenario, ∠ABC increases to become ∠A'B'C' due to extension of Zr-Zr distance and shortening of the Zr-X distance (see ∠A'B'C' in Fig. 12b). Among those four different connection modes, the 2, 3 and 4-atom sharing clusters are stiffer than the 1-atom sharing clusters [33,67]. Hence, as the tensile stress increases, more and more 1-atom shared clusters break apart (see Figs. 10a and 12c).

While Fig. 12d shows a typical cluster in the compressive stress state, the Zr-Zr pair bond length decreases with the increase of stress, "pushing" the two Zr-centred clusters to move close towards each other (Fig. 12d) until they start to "share" atoms, forming Zr-X-Zr linkage with angle of ∠DEF (see Fig. 12e). The distance between two central Zr atoms in MRO clusters with 4-atom-sharing connection is the smallest [33]. Further increasing the compressive stress, the Zr-Zr pair bond length decreases further and the two Zr-centred clusters finally become the one shown in Fig. 12f, where the two Zr atoms connect directly with a smaller bond angle, i.e., ∠D'E'F' in Fig. 12f. Hence, an obvious decrease in the percentage of 4-atom-sharing connection mode is observed in Fig. 10d.

5. Conclusions

We used *in situ* SEM imaging, SXTS plus EPSR modelling to study synergistically and systematically the evolution of SRO and MRO structures in a 5-element multicomponent Zr-based commercial glassy alloy at different stress states. The important findings of this research are:

1. We have demonstrated that the EPSR modelling is so far the most computationally efficient method for reconstructing the 3D atomic structure of the multicomponent MGs based on the experimentally collected total scattering data. Systematic and comprehensive analyses on the characteristics of the SRO and MRO structures and the decoupled 15 partial PDFs at each stress level reveal quantitatively how the SRO and MRO structures rearrange in 3D space in the tensile and compressive states.
2. Compared to the solute atom-centred VPs, the Zr-centred VPs have a higher CN, and the $\widehat{W}_6$ value for Zr atom is higher than that of the solute atoms. Therefore the Zr-centred atom clusters have a low degree of icosahedra and are preferred atom clusters to rearrange themselves in order to accommodate the tensile and compressive stresses.

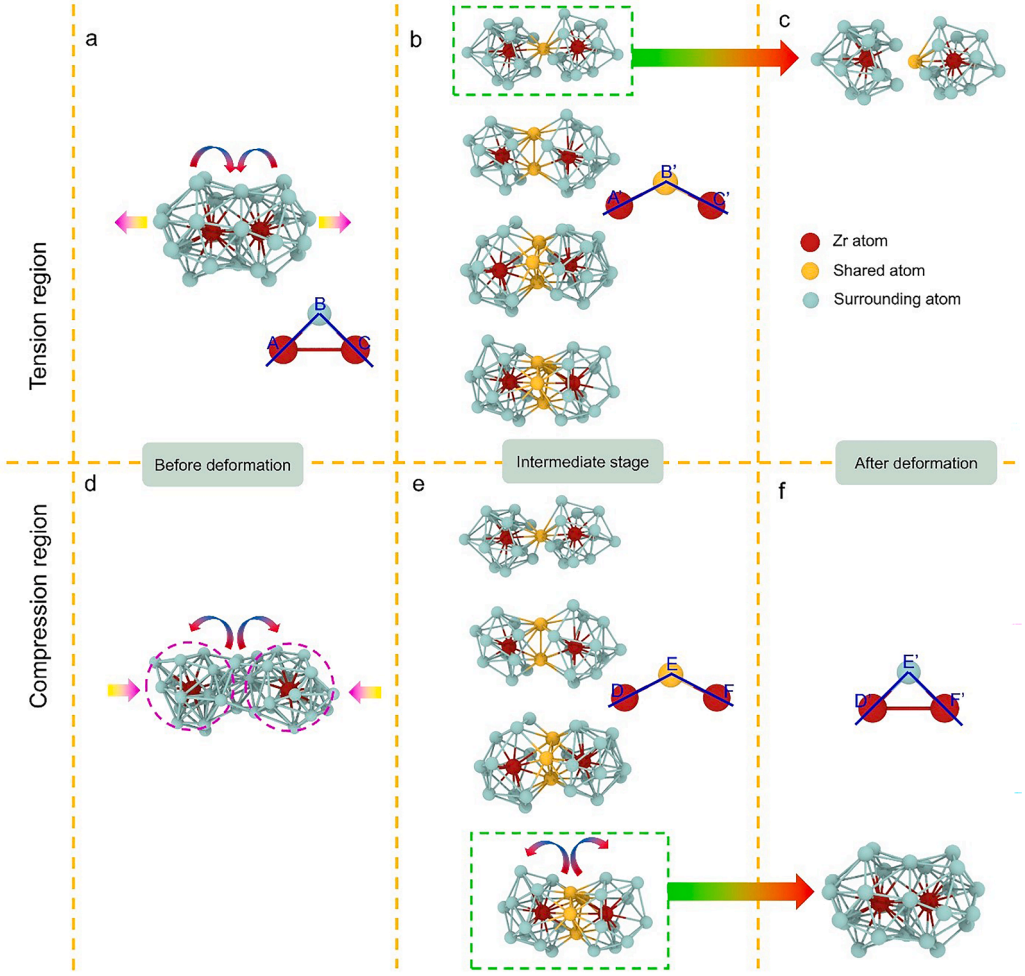

Fig. 12. A schematic, showing atomic structure evolution and reconfiguration in different stress states.

3. In this 5-element MG, the Zr-Zr pair is the dominant atom pair in controlling the elastic deformation. The yielding or breaking of Zr-Zr bonds plays a critical role in the initiation of shear bands in this Zr-based multicomponent MG.
4. The reconfigurations of the MRO clusters under different stress states are realised by changing the connection modes between the Zr-centred atom clusters. During the evolution, the coordinated changes of both bond angles and bond lengths of the Zr-centred clusters are the dominant factors in accommodating the tensile or compressive elastic stresses. Other solute-centred MRO clusters only play a minor role in the atomic structure evolution.
5. Under the tensile stress, both the bond length of Zr-Zr pairs and the Zr-S-Zr linkage increase with the tensile stress, and Zr-Zr bonds break when shear bands are nucleated. Upon further increasing the tensile stress, the MRO clusters with 1-atom-sharing mode break. By contrast, under the compressive stress, two Zr-centred clusters move towards each other, and MRO clusters would form *via* sharing atoms when the two central Zr atoms are close enough. The bond length of Zr-Zr pair continuously decreases as the compressive stress increases, resulting in the shared atoms moving away and the formation of Zr-Zr bond between these two central Zr atoms.

Data availability

Data will be made available on request.

CRediT authorship contribution statement

Shifeng Luo: Formal analysis, Funding acquisition, Investigation, Methodology, Writing – original draft. **Jia Chuan Khong:** Data curation, Formal analysis, Investigation, Methodology, Writing – review & editing. **Shi Huang:** Formal analysis, Investigation, Methodology, Writing – review & editing. **Guangyu Yang:** Writing – review & editing. **Jiawei Mi:** Conceptualization, Funding acquisition, Supervision, Writing – review & editing.

Declaration of competing interest

The authors declare no competing interests for this manuscript.

Acknowledgments

We would like to acknowledge the synchrotron X-ray beam time awarded by the Diamond Light Source (experiment No. EE7665-1, EE10440-1). J. Mi would like to thank the Royal Society for the Royal Society Industry Fellowship Award (2012-2016). S. Luo and S. Huang are grateful for the financial support from the China Scholarship Council for their PhD study at University of Hull, UK. S. Luo would also like to acknowledge the financial support from the National Natural Science Foundation of China (Grant No. 52204387), the State Key Laboratory of Solidification Processing in NWPU (Grant No. SKLSP202207) and the Fundamental Research Funds for the Central University (Grant No. JZ2022HGTA0326 and No. PA2022GDGP0029). The uses of GudrunX and EPSR software developed by the ISIS Neutron and Muon Source,

Science & Technology Facilities Council (STFC), especially the strong support given by Dr. Daniel T. Bowron and Dr. Tristan G. A. Youngs, as well as the uses of the Viper High Performance Computer of the University of Hull and the team for technical support on computing are gratefully acknowleaged.

Supplementary materials

Supplementary material associated with this article can be found, in the online version, at doi:10.1016/j.actamat.2024.119917.

References

[1] T.M. Pollock, Alloy design for aircraft engines, Nat. Mater. 15 (2016) 809–815.
[2] A.L. Greer, New horizons for glass formation and stability, Nat. Mater. 14 (2015) 542–546.
[3] A. Inoue, A. Takeuchi, Recent development and application products of bulk glassy alloys, Acta Mater. 59 (2011) 2243–2267.
[4] E. Ma, X. Wu, Tailoring heterogeneities in high-entropy alloys to promote strength-ductility synergy, Nat. Commun. 10 (2019) 5623.
[5] R. Aparicio-Fernández, H. Springer, A. Szczepaniak, H. Zhang, D. Raabe, *In-situ* metal matrix composite steels: effect of alloying and annealing on morphology, structure and mechanical properties of TiB_2 particle containing high modulus steels, Acta Mater. 107 (2016) 38–48.
[6] H. Pan, G. Qin, Y. Huang, Y. Ren, X. Sha, X. Han, Z.Q. Liu, C. Li, X. Wu, H. Chen, C. He, L. Chai, Y. Wang, J.F. Nie, Development of low-alloyed and rare-earth-free magnesium alloys having ultra-high strength, Acta Mater. 149 (2018) 350–363.
[7] W. Wang, Roles of minor additions in formation and properties of bulk metallic glasses, Prog. Mater. Sci. 52 (2007) 540–596.
[8] Z. Wu, M.C. Troparevsky, Y.F. Gao, J.R. Morris, G.M. Stocks, H. Bei, Phase stability, physical properties and strengthening mechanisms of concentrated solid solution alloys, Curr. Opin. Solid State Mater. Sci. 21 (2017) 267–284.
[9] D.B. Miracle, O.N. Senkov, A critical review of high entropy alloys and related concepts, Acta Mater. 122 (2017) 448–511.
[10] H.X. Li, Z.C. Lu, S.L. Wang, Y. Wu, Z.P. Lu, Fe-based bulk metallic glasses: glass formation, fabrication, properties and applications, Prog. Mater. Sci. 103 (2019) 235–318.
[11] A.L. Greer, Y.Q. Cheng, E. Ma, Shear bands in metallic glasses, Mater. Sci. Eng. R Rep. 74 (2013) 71–132.
[12] E.P. George, W.A. Curtin, C.C. Tasan, High entropy alloys: a focused review of mechanical properties and deformation mechanisms, Acta Mater. 188 (2020) 435–474.
[13] R. Liontas, M. Jafary-Zadeh, Q. Zeng, Y.W. Zhang, W.L. Mao, J.R. Greer, Substantial tensile ductility in sputtered Zr-Ni-Al nano-sized metallic glass, Acta Mater. 118 (2016) 270–285.
[14] D. Sorensen, E. Hintsala, J. Stevick, J. Pischlar, B. Li, D. Kiener, J.C. Myers, H. Jin, J. Liu, D. Stauffer, A.J. Ramirez, R.O. Ritchie, Intrinsic toughness of the bulk-metallic glass Vitreloy 105 measured using micro-cantilever beams, Acta Mater. 183 (2020) 242–248.
[15] R.L. Narayan, L. Tian, D. Zhang, M. Dao, Z.W. Shan, K.J. Hsia, Effects of notches on the deformation behavior of submicron sized metallic glasses: insights from *in situ* experiments, Acta Mater. 154 (2018) 172–181.
[16] T.C. Pekin, J. Ding, C. Gammer, B. Ozdol, C. Ophus, M. Asta, R.O. Ritchie, A. M. Minor, Direct measurement of nanostructural change during *in situ* deformation of a bulk metallic glass, Nat. Commun. 10 (2019) 2445.
[17] C. Ebner, J. Rajagopalan, C. Lekka, C. Rentenberger, Electron beam induced rejuvenation in a metallic glass film during *in-situ* TEM tensile straining, Acta Mater. 181 (2019) 148–159.
[18] Q.P. Cao, J.W. Liu, K.J. Yang, F. Xu, Z.Q. Yao, A. Minkow, H.J. Fecht, J. Ivanisenko, L.Y. Chen, X.D. Wang, S.X. Qu, J.Z. Jiang, Effect of pre-existing shear bands on the tensile mechanical properties of a bulk metallic glass, Acta Mater. 58 (2010) 1276–1292.
[19] C.Q. Chen, Y.T. Pei, J.T.M. De Hosson, Effects of size on the mechanical response of metallic glasses investigated through *in situ* TEM bending and compression experiments, Acta Mater. 58 (2010) 189–200.
[20] Y.J. Huang, J.C. Khong, T. Connolley, J. Mi, *In situ* study of the evolution of atomic strain of bulk metallic glass and its effects on shear band formation, Scr. Mater. 69 (2013) 207–210.
[21] Y. Huang, J.C. Khong, T. Connolley, J. Mi, The onset of plasticity of a Zr-based bulk metallic glass, Int. J. Plast. 60 (2014) 87–100.
[22] Y. Huang, J.C. Khong, T. Connolley, J. Mi, Understanding the deformation mechanism of individual phases of a ZrTi-based bulk metallic glass matrix composite using *in situ* diffraction and imaging methods, Appl. Phys. Lett. 104 (2014) 031912.
[23] H.F. Poulsen, J.A. Wert, J. Neuefeind, V. Honkimäki, M. Daymond, Measuring strain distributions in amorphous materials, Nat. Mater. 4 (2005) 33–36.
[24] H.S. Shahabi, S. Scudino, I. Kaban, M. Stoica, U. Rütt, U. Kühn, J. Eckert, Structural aspects of elasto-plastic deformation of a Zr-based bulk metallic glass under uniaxial compression, Acta Mater. 95 (2015) 30–36.
[25] L. Wang, Y. Zhao, L. Wang, Z. Nie, B. Wang, Y. Xue, H. Zhang, H. Fu, D.E. Brown, Y. Ren, *In-situ* synchrotron X-ray diffraction study of dual-step strain variation in laser shock peened metallic glasses, Scr. Mater. 149 (2018) 112–116.
[26] X. Tong, G. Wang, J. Bednarčík, Y.D. Jia, I. Hussain, J. Yi, Z.H. Stachurski, Q. J. Zhai, Structural evolution in a metallic glass pillar upon compression, Mater. Sci. Eng. A 721 (2018) 8–13.
[27] J.C. Ye, J. Lu, C.T. Liu, Q. Wang, Y. Yang, Atomistic free-volume zones and inelastic deformation of metallic glasses, Nat. Mater. 9 (2010) 619–623.
[28] H. Lou, Z. Zeng, F. Zhang, S. Chen, P. Luo, X. Chen, Y. Ren, V.B. Prakapenka, C. Prescher, X. Zuo, T. Li, J. Wen, W.H. Wang, H. Sheng, Q. Zeng, Two-way tuning of structural order in metallic glasses, Nat. Commun. 11 (2020) 314.
[29] F. Zhu, A. Hirata, P. Liu, S. Song, Y. Tian, J. Han, T. Fujita, M. Chen, Correlation between local structure order and spatial heterogeneity in a metallic glass, Phys. Rev. Lett. 119 (2017) 215501.
[30] D. Ma, A.D. Stoica, X.L. Wang, Power-law scaling and fractal nature of medium-range order in metallic glasses, Nat. Mater. 8 (2009) 30–34.
[31] D. Ma, A.D. Stoica, X.L. Wang, Z.P. Lu, B. Clausen, D.W. Brown, Elastic moduli inheritance and the weakest link in bulk metallic glasses, Phys. Rev. Lett. 108 (2012) 085501.
[32] N. Mattern, J. Bednarčik, S. Pauly, G. Wang, J. Das, J. Eckert, Structural evolution of Cu-Zr metallic glasses under tension, Acta Mater. 57 (2009) 4133–4139.
[33] S. Liu, L. Wang, J. Ge, Z. Wu, Y. Ke, Q. Li, B. Sun, T. Feng, Y. Wu, J.T. Wang, H. Hahn, Y. Ren, J.D. Almer, X.L. Wang, S. Lan, Deformation-enhanced hierarchical multiscale structure heterogeneity in a Pd-Si bulk metallic glass, Acta Mater. 200 (2020) 42–55.
[34] A.K. Soper, Empirical potential Monte Carlo simulation of fluid structure, Chem. Phys. 202 (1996) 295–306.
[35] A.K. Soper, Empirical Potential Structure Refinement-A User's Guide, ISIS Rutherfoord Appleton Labortory, Didcot UK, 2006.
[36] B. Kalkan, B. Godwal, S.V. Raju, R. Jeanloz, Local structure of molten $AuGa_2$ under pressure: evidence for coordination change and planetary implications, Sci. Rep. 8 (2018) 6844.
[37] Y. Zhou, T. Yamaguchi, K. Ikeda, K. Yoshida, T. Otomo, C. Fang, W. Zhang, F. Zhu, Dihydrogen bonds in aqueous $NaBD_4$ solution by neutron and X-ray diffraction, J. Phys. Chem. Lett. 11 (2020) 1622–1628.
[38] S. Lenton, N.H. Rhys, J.J. Towey, A.K. Soper, L. Dougan, Highly compressed water structure observed in a perchlorate aqueous solution, Nat. Commun. 8 (2017) 919.
[39] S. Huang, S. Luo, L. Qin, D. Shu, B. Sun, A.J.G. Lunt, A.M. Korsunsky, J. Mi, 3D local atomic structure evolution in a solidifying Al-0.4Sc dilute alloy melt revealed in operando by synchrotron X-ray total scattering and modelling, Scr. Mater. 211 (2022) 114484.
[40] S. Luo, J.C. Khong, D. Daisenberger, S. Huang, P.F. Mcmillan, J. Mi, Synchrotron x-ray total scattering and modeling study of high-pressure-induced inhomogeneous atom reconfiguration in an equiatomic $Zr_{50}Cu_{50}$ metallic glassy alloy, Phys. Rev. B 105 (2022) 064203.
[41] A. Peker, W.L. Johnson, A highly processable metallic glass: $zr_{41.2}Ti_{13.8}Cu_{12.5}Ni_{10.0}Be_{22.5}$, Appl. Phys. Lett. 63 (1993) 2342–2344.
[42] M. Telford, The case for bulk metallic glass, Mater. Today 7 (2004) 36–43.
[43] M. Drakopoulos, T. Connolley, C. Reinhard, R. Atwood, O. Magdysyuk, N. Vo, M. Hart, L. Connor, B. Humphreys, G. Howell, S. Davies, T. Hill, G. Wilkin, U. Pedersen, A. Foster, N. De Maio, M. Basham, F. Yuan, K. Wanelik, I12: the joint engineering, environment and processing (JEEP) beamline at diamond light source, J. Synchrotron Radiat. 22 (2015) 828–838.
[44] J. Filik, A.W. Ashton, P.C.Y. Chang, P.A. Chater, S.J. Day, M. Drakopoulos, M. W. Gerring, M.L. Hart, O.V. Magdysyuk, S. Michalik, A. Smith, C.C. Tang, N. J. Terrill, M.T. Wharmby, H. Wilhelm, Processing two-dimensional X-ray diffraction and small-angle scattering data in DAWN 2, J. Appl. Crystallogr. 50 (2017) 959–966.
[45] A.K. Soper, GudrunN and GudrunX: programs for correcting raw neutron and X-ray diffraction data to differential scattering cross section. Swindon UK, Sci. Technol. Facil. Counc. (2011).
[46] T. Yamaguchi, K. Fujimura, K. Uchi, K. Yoshida, Y. Katayama, Structure of water from ambient to 4GPa revealed by energy-dispersive X-ray diffraction combined with empirical potential structure refinement modeling, J. Mol. Liq. 176 (2012) 44–51.
[47] A.K. Soper, The radical distribution functions of water and ice from 220 to 673K and at pressures up to 400MPa, Chem. Phys. 258 (2000) 121–137.
[48] X. Hui, H.Z. Fang, G.L. Chen, S.L. Shang, Y. Wang, J.Y. Qin, Z.K. Liu, Atomic structure of Zr41.2Ti13.8Cu12.5Ni10Be22.5 bulk metallic glass alloy, Acta Mater. 57 (2009) 376–391.
[49] D.B. Miracle, The efficient cluster packing model - An atomic structural model for metallic glasses, Acta Mater. 54 (2006) 4317–4336.
[50] P.R.T. Wolde, M.J. Ruiz-Montero, D. Frenkel, Numerical calculation of the rate of crystal nucleation in a Lennard-Jones system at moderate undercooling, J. Chem. Phys. 104 (1996) 9932–9947.
[51] P.J. Steinhardt, D.R. Nelson, M. Ronchetti, Bond-orientational order in liquids and glasses, Phys. Rev. B 28 (1983) 784–805.
[52] Y.Q. Cheng, A.J. Cao, E. Ma, Correlation between the elastic modulus and the intrinsic plastic behavior of metallic glasses: the roles of atomic configuration and alloy composition, Acta Mater. 57 (2009) 3253–3267.
[53] J. Ding, E. Ma, Computational modeling sheds light on structural evolution in metallic glasses and supercooled liquids, npj, Comput. Mater. 3 (2017) 9.
[54] S.P. Pan, J.Y. Qin, W.M. Wang, T.K. Gu, Origin of splitting of the second peak in the pair-distribution function for metallic glasses, Phys. Rev. B 84 (2011) 092201.
[55] J. Du, B. Wen, Composition-structure-property correlations of complex metallic alloys described by the "cluster-plus-glue-atom" model, Appl. Mater. Today 7 (2017) 13–46.
[56] P. Ganesh, M. Widom, *Ab initio* simulations of geometrical frustration in supercooled liquid Fe and Fe-based metallic glass, Phys. Rev. B 77 (2008) 014205.

[57] H.W. Sheng, W.K. Luo, F.M. Alamgir, J.M. Bai, E. Ma, Atomic packing and short-to-medium-range order in metallic glasses, Nature 439 (2006) 419–425.
[58] Y.Q. Cheng, E. Ma, H.W. Sheng, Atomic level structure in multicomponent bulk metallic glass, Phys. Rev. Lett. 102 (2009) 245501.
[59] D. Ma, A.D. Stoica, L. Yang, X.L. Wang, Z.P. Lu, J. Neuefeind, M.J. Kramer, J. W. Richardson, T. Proffen, Nearest-neighbor coordination and chemical ordering in multicomponent bulk metallic glasses, Appl. Phys. Lett. 90 (2007) 211908.
[60] R.L. Mcgreevy, Reverse Monte Carlo modeling, J. Phys. Condens. Matter 13 (2001) R877–R913.
[61] M.E. Blodgett, K.F. Kelton, Estimated partial pair correlation functions in Cu-Zr liquids, J. Non Cryst. Solids 412 (2015) 66–71.
[62] X. Wang, H. Zhang, J.F. Douglas, The initiation of shear band formation in deformed metallic glasses from soft localized domains, J. Chem. Phys. 155 (2021) 204504.
[63] C. Geng, B. Huang, N. Zhang, J. Yi, Q. Wang, Y. Jia, F. Li, J. Luan, X. Hou, W. Huang, Q. Yuan, G. Wang, W. Wang, Evolution of local densities during shear banding in Zr-based metallic glass micropillars, Acta Mater. 235 (2022) 118068.
[64] L.S. Huo, J.F. Zeng, W.H. Wang, C.T. Liu, Y. Yang, The dependence of shear modulus on dynamic relaxation and evolution of local structural heterogeneity in a metallic glass, Acta Mater. 61 (2013) 4329–4338.
[65] Y. Shao, K. Yao, M. Li, X. Liu, Two-zone heterogeneous structure within shear bands of a bulk metallic glass, Appl. Phys. Lett. 103 (2013) 171901.
[66] S. Liu, W. Dong, Z. Ren, J. Ge, S. Fu, Z. Wu, J. Wu, Y. Lou, W. Zhang, H. Chen, W. Yin, Y. Ren, J. Neuefeind, Z. You, Y. Liu, X.L. Wang, S. Lan, Medium-range order endows a bulk metallic glass with enhanced tensile ductility, J. Mater. Sci. Technol. 159 (2023) 10–20.
[67] J. Ding, E. Ma, M. Asta, R.O. Ritchie, Second-nearest-neighbor correlations from connection of atomic packing motifs in metallic glasses and liquids, Sci. Rep. 5 (2015) 17429.
[68] H.L. Peng, M.Z. Li, W.H. Wang, Structural signature of plastic deformation in metallic glasses, Phys. Rev. Lett. 106 (2011) 135503.
[69] M.Z. Li, Correlation between local atomic symmetry and mechanical properties in metallic glasses, J. Mater. Sci. Technol. 30 (2014) 551–559.
[70] M. Lee, C.M. Lee, K.R. Lee, E. Ma, J.C. Lee, Networked interpenetrating connections of icosahedra: effects on shear transformations in metallic glass, Acta Mater. 59 (2011) 159–170.